IEEE Photonics Journal
An IEEE Photonics Society Publication

Open Access

Inverse Scattering Method Design of Regrowth-Free Single-Mode Semiconductor Lasers Using Pit Perturbations for Monolithic Integration

Volume 10, Number 05, September 2018

Kevin Shortiss
Mohamad Dernaika
Ludovic Caro
Masoud Seifikar
Frank H. Peters

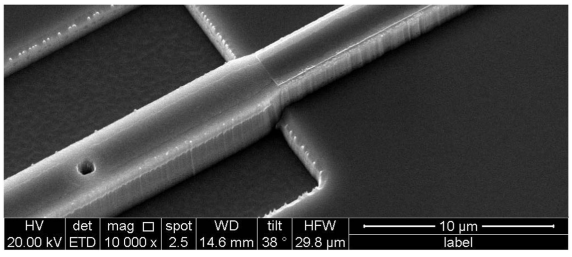

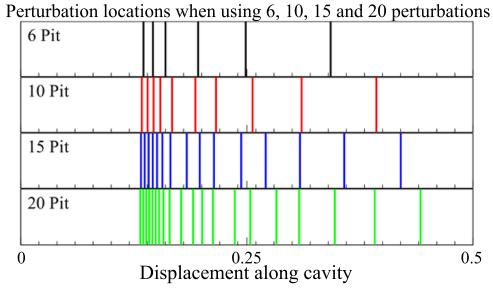

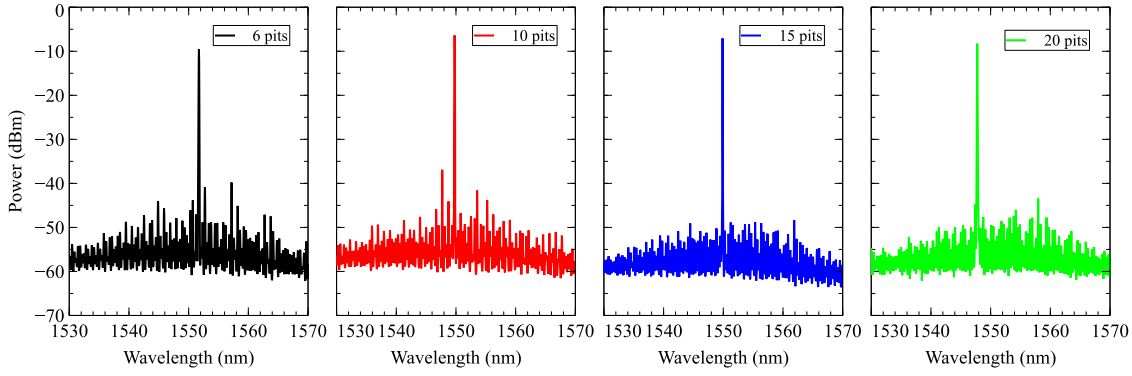

DOI: 10.1109/JPHOT.2018.2873048
1943-0655 © 2018 IEEE

Inverse Scattering Method Design of Regrowth-Free Single-Mode Semiconductor Lasers Using Pit Perturbations for Monolithic Integration

Kevin Shortiss,[1,2] **Mohamad Dernaika**,[1,3] **Ludovic Caro**,[1,2] **Masoud Seifikar**,[1,2] **and Frank H. Peters**[1,2]

[1]Integrated Photonics Group, Tyndall National Institute, Cork T12R5CP, Ireland
[2]Department of Physics, University College Cork, Cork T12YN60, Ireland
[3]Department of Electrical and Electronic Engineering, University College Cork, Cork T12YN60, Ireland

DOI:10.1109/JPHOT.2018.2873048

Manuscript received September 17, 2018; accepted September 25, 2018. Date of publication October 1, 2018; date of current version October 12, 2018. This work was supported by Science Foundation Ireland under Grant SFI 13/IA/1960. Corresponding author: Kevin Shortiss (e-mail: kshortiss@gmail.com). This paper has supplementary downloadable material available at http://ieeexplore.ieee.org.

Abstract: An inverse scattering method is used to design regrowth-free single-mode lasers, using etch depth insensitive pits as perturbations in the laser cavity. These pit perturbations are circular holes etched into the waveguide of each laser to a depth 0.8 μm below the quantum wells in the laser material, and are used in place of the etch depth sensitive slots more commonly implemented for optical feedback in photonic integrable lasers. We compare the number of these pit perturbations required to achieve the target wavelength of the devices, and report strongly single mode lasers (greater than 40 dB). Devices were then designed to lase at wavelengths between 1545 nm and 1565 nm, to demonstrate the wavelength accuracy of the designs. Thermal tuning was used to tune device wavelength over 2 nm, while maintaining side mode suppression ratios greater than 30 dB.

Index Terms: Semiconductor lasers, photonic integrated circuits.

1. Introduction

The fabrication processes of distributed feedback lasers or distributed Bragg reflector (DBR) lasers can be expensive and time consuming. In contrast, semiconductor lasers free from re-growth steps and that use standard contact UV lithography greatly reduce the time and cost involved in fabricating devices. As a result, much research has been focused on designing devices and processes which eliminate the need for high precision lithography and epitaxial regrowth.

Slotted Fabry-Pérot lasers [1]–[3] are one such example, which use slots etched into the ridge of the waveguide to provide feedback and mode selectivity. Slotted Fabry-Pérot lasers can provide high side-mode suppression ratios (SMSR) and low linewidth, however the slots which provide the wavelength selectivity of the laser are etch depth dependent [3]–[5]. As a result, etch stop layers are required to accurately control the reflectivity of the slots, and the anisotropicity of chemical etches [6] can lead to different results across a wafer.

In this paper, we demonstrate regrowth-free single moded lasers which use etch depth insensitive pits [5] etched into the waveguide of the slave laser. The pits are etched deep into the material, and hence the amount of reflection introduced into the laser cavity does not vary strongly with etch depth, unlike the slots. High SMSR (37 dB) and low linewidth have been previously demonstrated using 30 pits in an integrated DBR like mirror [7]. In this paper, single moded lasing is achieved by using pits as local perturbations placed as described by an inverse scattering technique [8]. The inverse scattering technique used has successfully been demonstrated using slots [9] and side wall gratings [10], however in both cases either high resolution e-beam or high reflectance (HR) coatings were applied to the facets of the devices. The design of the devices presented uses Fourier techniques to specify the position each pit should be placed, in order to approximate a target threshold gain function.

Now we show that deeply etched waveguide pits, which require no epitaxial regrowth and use standard contact UV lithography, can achieve similar results with higher fabrication tolerances and lower fabrication costs. Each pit is etched down to a depth of 0.8 μm beyond the quantum wells (QWs) in the centre of the ridge waveguide of the laser, and is circular with a 1 μm diameter. Unlike the reported slotted inverse scattering lasers, the side wall roughness and etch depth of the perturbations used isn't as integral to the device's operation, as the deeply etched pits are used as local perturbations in the laser's waveguide. As a result, devices using pit perturbations have higher device yield than slotted devices, however suffer slightly in performance due to the rudimentary perturbations used, which lead to additional scattering losses. Standard commercial AlInGaAs material grown on a InP substrate was used for the fabrication of the devices, and the details of the epitaxial structure used can be found in the supplementary material supporting this paper.

We present the results of our investigation into the required number of pits to achieve the target wavelength, and report laser designs with SMSRs of greater than 40 dB. Optimal performance was achieved with devices featuring 15 pit perturbations, and hence using 15 pit devices we also demonstrate the design capability to target different specific wavelengths within the laser materials gain bandwidth.

A brief outline of the inverse scattering technique is described in Section 2 below, and results, discussion and comparison between the theory and design of the devices are presented in Section 3.

2. Spectral Engineering With an Inverse Scattering Method

The inverse scattering method used to achieve single mode lasing was first presented by O'Brien *et al.* in [11], and was later expanded and described in more detail in [8]. The strength of using the inverse scattering method over a regular periodic grating is the ability to engineer the output spectrum of a semiconductor laser using simple perturbations along the lasers ridge. Single mode, dual mode [9], [12] and optical comb generation [13], [14] have all been modeled using the inverse scattering method. Experimental results for single mode devices have shown SMSRs of up to 50 dB, however the fabricated devices used HR coated facets with several etched slots.

In this paper, pit perturbations [5] are used instead of slots due to the advantages mentioned in the previous section. When the modeling of the devices was performed, the method used was mostly unchanged from O'Brien's 2011 paper, and as a result only an outline of the method is presented in the section below. The differences in the assumptions due to the pit perturbations rather than slots used in [8] and this work are highlighted within the section.

2.1 Inverse Scattering Method

To achieve single mode lasing, the inverse scattering method attempts to lower the threshold gain of a target mode more than the other competing longitudinal Fabry-Pérot modes in the laser cavity. This is achieved by introducing N perturbations into the laser cavity, where each perturbation changes the effective index of the supported optical mode by $\Delta n = n_1 - n_2$, as shown in Fig. 1, where n_1 is the effective refractive index of the waveguide, and n_2 is the effective refractive index

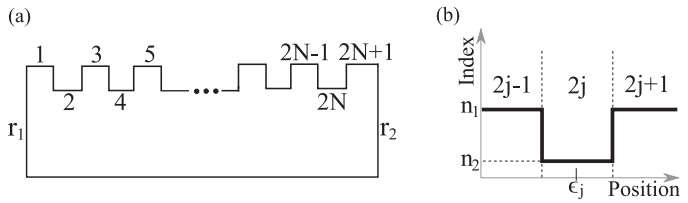

Fig. 1. (a) Illustration of N perturbations introduced to the cavity, creating $2N + 1$ sections. (b) Illustration of a single perturbation, where ϵ_j gives the centre of the perturbation.

of the perturbation section. The method calculates the locations of each perturbation, to minimise the threshold gain of the target mode.

We can describe each section j of the cavity using one dimensional transmission matrices [15]. Multiplying the transmission matrices in the correct order, we find the total transmission matrix **T** for the cavity, excluding the two end facets. It can be shown that the four elements T_{11}, T_{12}, T_{21} and T_{22} of the total transmission matrix **T** of the laser cavity due to the N perturbations are given by:

$$T_{11} = e^{-i\sum_{k=1}^{2N+1}\theta_k}, \tag{1}$$

$$T_{12} = -i\frac{\Delta n}{n}\sum_{k=1}^{N}\sin(\theta_{2k})\, e^{j\left(-\sum_{l=1}^{2k-1}\theta_l+\sum_{l=2k+1}^{2N+1}\theta_l\right)}, \tag{2}$$

$$T_{21} = -i\frac{\Delta n}{n}\sum_{k=1}^{N}\sin(\theta_{2k})\, e^{j\left(\sum_{l=1}^{2k-1}\theta_l-\sum_{l=2k+1}^{2N+1}\theta_l\right)}, \tag{3}$$

$$T_{22} = e^{j\sum_{k=1}^{2N+1}\theta_k}, \tag{4}$$

where here we are only including the first order perturbation in Δn. In the above, θ_i is the phase change experienced by the electric field due to propagation through section i, given by $\theta_i = n_i L_i k_z$. Here, k_z is the wavenumber in free space, and L_i is the length of section i. Note that, up to first order, T_{11} and T_{22} are unchanged from the unperturbed case, which we can assume true provided that $N\Delta n/n \ll 1$ holds. The threshold condition of the laser cavity from the transmission matrix **T** can then be written as:

$$T_{11} - T_{22}r_1r_2 = T_{21}r_1 - T_{12}r_2. \tag{5}$$

Here, r_1 and r_2 are the reflections seen by the electric field at the facets on the left hand side and the right hand side of the device, respectively. Using the definition of the elements of **T** in eq. (5) gives:

$$1 = r_1r_2e^{2i\sum_{j=1}^{2N+1}\theta_j} + i\frac{\Delta n}{n}\sum_{j=1}^{N}\sin\theta_{2j}\left[r_1e^{2i\phi_j^-} + r_2e^{2i\phi_j^+}\right]. \tag{6}$$

The terms ϕ_j^- and ϕ_j^+ introduced in eq. (6) are the complex optical path lengths from the centre of perturbation j to the left and right facets, respectively. By definition, they are:

$$\phi_j^- = \frac{\theta_{2j}}{2} + \sum_{k=1}^{2j-1}\theta_k, \tag{7}$$

$$\phi_j^+ = \frac{\theta_{2j}}{2} + \sum_{k=2j+1}^{2N+1}\theta_k. \tag{8}$$

By expanding θ_j, ϕ_j^- and ϕ_j^+ into real and imaginary parts, the gain required for each mode m of the laser gain be derived from eq. (6). Labeling the centre of each perturbation ϵ_j (as in Fig. 1(b)),

and assuming constant gain across the device, we can relate the imaginary parts of $\phi_j^{\pm}$ to the fractional position of the perturbation along the cavity ϵ_j by writing:

$$\mathrm{Im}\left[\phi_j^-\right] = \left(\frac{1}{2} + \epsilon_j\right) \sum_{k=0}^{2N+1} \theta_k, \tag{9}$$

$$\mathrm{Im}\left[\phi_j^+\right] = \left(\frac{1}{2} - \epsilon_j\right) \sum_{k=0}^{2N+1} \theta_k, \tag{10}$$

where $-1/2 < \epsilon_j < 1/2$. For the trivial case of $\Delta n = 0$, the threshold gain $\gamma_m^{(0)}$ required for each mode in the cavity is identical:

$$\gamma_m^{(0)} = \frac{1}{L_c} \ln \frac{1}{|r_1 r_2|}. \tag{11}$$

For non trivial perturbations, the first order perturbation to the gain γ_m can be written as:

$$\gamma_m^{(1)} = \frac{1}{L_c\sqrt{|r_1 r_2|}} \sum_{j=1}^{N} \sin\theta_{2j} \left[|r_1| \sin\left(2\,\mathrm{Re}\left[\phi_j^-\right]\right) e^{\epsilon_j \gamma_m^{(0)} L_c} + |r_2| \sin\left(2\,\mathrm{Re}\left[\phi_j^+\right]\right) e^{-\epsilon_j \gamma_m^{(0)} L_c} \right]. \tag{12}$$

In the above expression, the phase change due to the reflections at the facets has been ignored. In general, eg. (12) will vary for each mode m. The amplitude of the gain modulation is determined by the function

$$f(\epsilon_j) = |r_1| \sin\left(2\,\mathrm{Re}\left[\phi_j^-\right]\right) e^{\epsilon_j \gamma_m^{(0)} L_c} + |r_2| \sin\left(2\,\mathrm{Re}\left[\phi_j^+\right]\right) e^{-\epsilon_j \gamma_m^{(0)} L_c}. \tag{13}$$

The function f determines the magnitude of the change in threshold due to each perturbation ϵ_j, as well as dictating the location of the centre of perturbations along the laser cavity. In previous works [14], it was assumed that $\sin(2\phi_j^+) = -\sin(2\phi_j^-)$, which is true for weakly perturbed cases. Here, we don't included this assumption and instead work with the full expression, as the purpose of this study was to investigate the effect of increasing the number of perturbations in the cavity.

To design a device, we start by choosing a target threshold modulation function, which will give the envelope of the threshold gain. An ideal function for single mode devices is one which greatly reduces the target mode's threshold gain, and leaves the other modes untouched. If the target mode of the laser is m_0, then $-\mathrm{sinc}(\pi\Delta m/m)$ gives a minimum threshold gain when $\Delta m = m - m_0 = 0$, and leaves all other Fabry-Pérot modes untouched.

We wish to place perturbations along the cavity of the laser, and have them select the frequency components in reciprocal space which represent the target function $-\mathrm{sinc}(\pi\Delta m/m)$. In practice, there are only a finite number of the cavities resonances that fit in the gain bandwidth of the laser's material, and resonances away from the gain center effect the output spectrum of the laser less. To account for this, a finite number of cavity resonances are included in the final expression for the target threshold modulation function, and the function is scaled by an exponential decay $\exp\left[-\pi\tau^2\Delta m^2\right]$. The spacing and the target threshold modulation function g is re-written as:

$$g = \exp\left[-\pi\tau^2\Delta m^2\right] \sum_{n=-K}^{K} \mathrm{sinc}\left(\Delta \mathrm{m} - \mathrm{na}\right). \tag{14}$$

Here, τ determines the decay of the threshold gain modulation, and we include resonances every a cavity modes. The constant K limits the number of resonances included in the numerical calculation, and was chosen to be arbitrarily large.

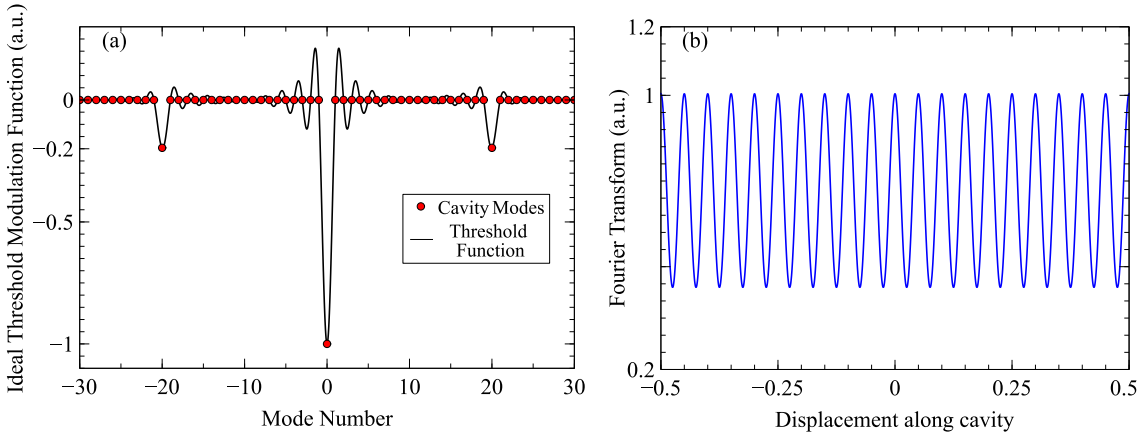

Fig. 2. (a) Ideal threshold modulation function, as given by eq. (14) for $a = 20$ and $\tau = 0.036$. The red points give the value at each of the cavity modes. (b) Fourier transform of the ideal threshold modulation function shown in (a).

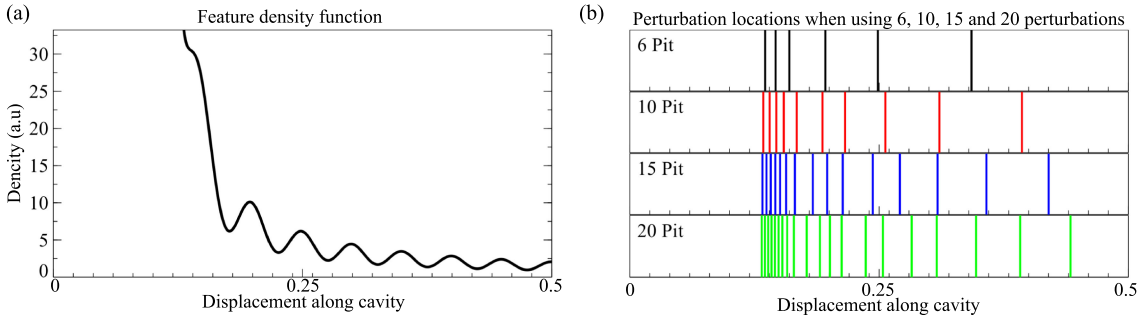

Fig. 3. (a) Feature density function for the etched facet side of the device only, for a 1 mm long laser cavity with the parameters in Fig. 2. The x-axis is scaled so that 0.0 is the physical centre of the cavity, and +0.5 is right facet. The grating centre was at a displacement of 0.118267 along the cavity, due to the mismatched reflections of the cleaved and etched facets. (b) Illustration of the perturbation positions found using the inverse scattering method when 6, 10, 15 and 20 perturbations are used.

The Fourier transform of our desired function g from eq. (14) is then given as a series of Gaussian distributions defined by:

$$\Gamma(\epsilon) = \sum_{n=-K}^{K} \exp\left[-\pi(\epsilon - n/a)^2/\tau^2\right] \tag{15}$$

Fig. 2(a) shows the desired threshold modulation function f for $a = 20$, $\tau = 0.036$, and Fig. 2(b) shows the approximated Fourier transform for the threshold modulation function in (a), as given by eq. (15).

To determine the index pattern required to generate the target threshold modulation function, we need to account for the positions required to approximate the Fourier transform of our desired threshold function, while also accounting for how the magnitude of the modulation of the threshold gain function $f(\epsilon)$ varies along the cavity. The product of $\Gamma_n(\epsilon)$ and $f(\epsilon)^{-1}$ (called the feature density function) takes both of these into consideration, and is plotted in Fig. 3(a) for $\Delta n = 0.0075$. The pit widths were measured as 1 μm, and hence the perturbations were assumed to be 1 μm in length. In order to discretise the feature density function, we determine solutions to the following expression:

$$A \sum_{n} \int_{\epsilon_{\min}}^{\epsilon_j} [f(x)]^{-1} \Gamma_n(x) dx = j - \frac{1}{2} \tag{16}$$

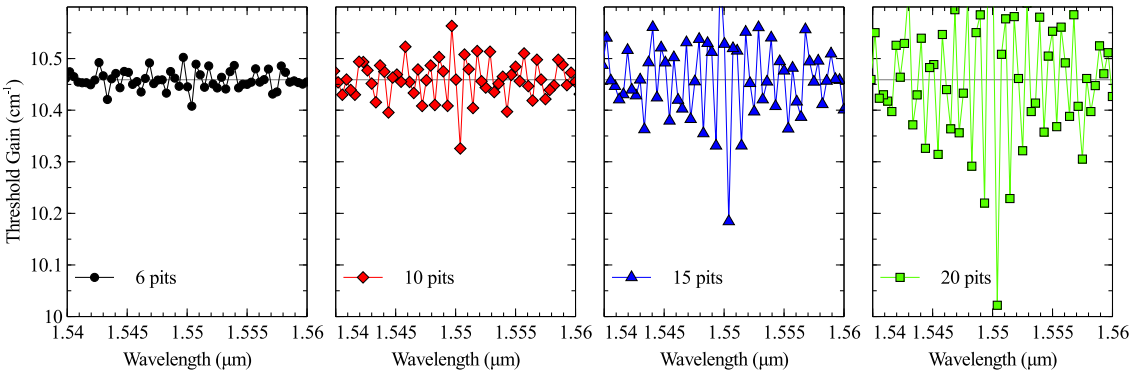

Fig. 4. Calculated threshold gain versus wavelength as given by eq. (12) for the gratings shown in Fig. 3(b). The solid horizontal line in each plot is the calculated unperturbed threshold gain of the laser cavity, i.e., $\gamma_m^{(0)} = 10.46\,\mathrm{cm}^{-1}$.

for $j = 1, 2, ..., N$, and with A normalised to account for the number of perturbations in the cavity. The lower bound ϵ_{min} is chosen to ensure that not all features are placed at the zero of $f(x)$. To maximise the effect of each perturbation, after the perturbation positions are have been determined with eq. (16), the positions are shifted slightly to meet the condition $\sin(2\,\mathrm{Re}[\phi_j^{\pm}]) = \pm 1$. Here, $+$ is used for perturbations on the right hand side of the zero of $f(x)$, and $-$ for the perturbations on the left hand side.

2.2 Device Design

As knowing the exact optical path length between perturbations and the facets is pivotal in the above, metal covered deep etched facets (defined by the same lithography step which created the perturbations) were used on one side of the devices to accurately control the relative distance of each perturbation to this etched facet. The other facet was an un-coated cleaved facet, which had a positional tolerance of $\pm 10\,\mu$m. The metal covered deep etched facet's reflection was estimated to be 45%, compared with the uncoated facet's reflection of 27.5%. Due to this mismatch in the reflective strengths of the facets, the centre of the feature density function shifts. For arbitrary r_1 and r_2, the centre is given by $\ln[r_2/r_1]/2\ln[1/r_1 r_2]$, which can be found by finding the zero of $f(x)$ in the weakly perturbed case.

As only the etched facet's location could be accurately controlled, single sided gratings were designed. Fig. 3(b) shows the perturbation locations for 6, 10, 15 and 20 pit devices, for $\epsilon_{\mathrm{min}} = 0.0125$, with $\Delta n = 0.0075$. As the number of perturbations is increased, notably more are located close to the zero of the $f(x)$ function. As we increase the number of perturbations included, the wavelength control and selectivity should also increase. There are two main limits however to the number of perturbations which can be introduced: the loss per pit, and the physical size of the pits.

The corresponding threshold gains calculated for the gratings in Fig. 3(b) are plotted in Fig. 4. As the number of perturbations is increased in the model, the threshold of the target mode significantly decreases – however, the loss per pit is not included in these calculations. As a result, indefinitely increasing the number of pits does not increase the SMSR or output lasing power of the targeted mode.

3. Device Results and Discussion

The devices were fabricated on standard commercial material with 5 $Al_{0.24}GaIn_{0.71}As$ QWs grown on InP. The details of thicknesses and the structure of the epitaxial layers of the material can be found in the supplementary material supporting this paper. The fabrication process used only two etch depths in order to reduce the time and cost involved.

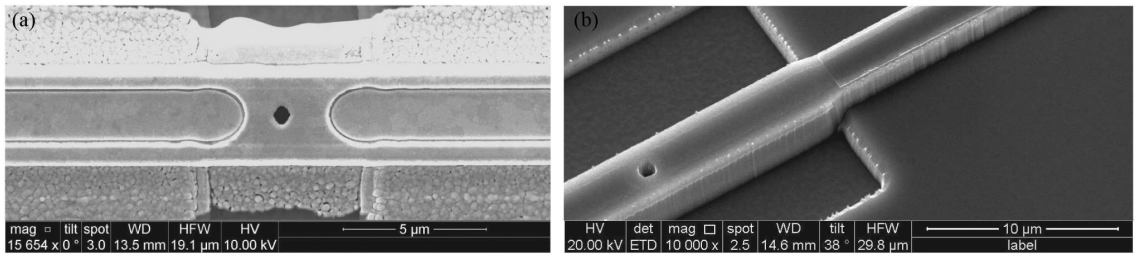

Fig. 5. (a) Scanning electron microscope image of one of the pits used as perturbations in the waveguide. (b) View of the sidewall of a test device after the second etch step in the process, showing the two different etch depths used in fabrication, with a pit perturbation visible in the bottom left of the image.

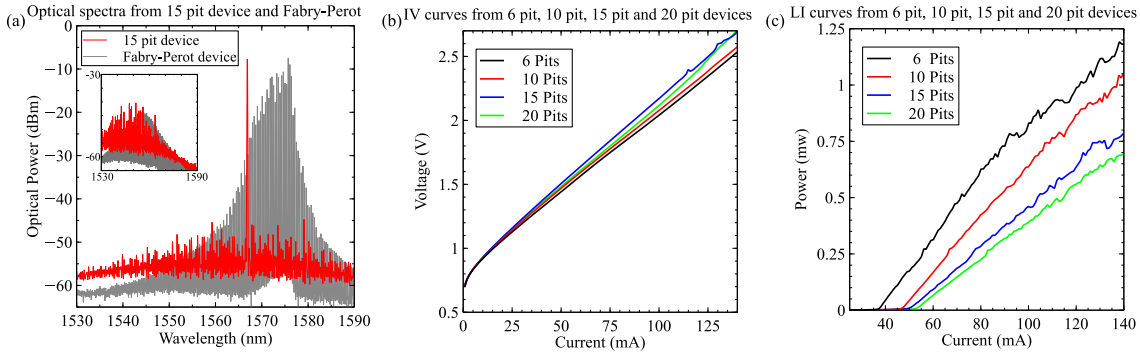

Fig. 6. (a) Comparison between the spectra of a FP cavity and a 15 pit device at 140 mA, at 20 °C. Both devices were 1 mm long, with one cleaved facet and one metal covered etched facet. Inset: Optical spectrum from the same two devices just below threshold. (30 mA for the FP device, and 47 mA for the 15 pit device). (b) A plot of voltage versus current for 1 mm long devices with 6, 10, 15 and 20 pits. (c) LI curves for the devices plotted in (b). The thresholds of the devices were 37 mA, 46 mA, 49 mA, and 53 mA respectively. The kinks in the curves are due to vibrations in the optical fibre used to collect the light.

Each patterning step of the fabrication of the devices used contact photo lithography to define the areas for deposition/etching of the devices. In brief, the fabrication process of the devices was as follows; first, plasma-enhanced chemical vapor deposition (PECVD) of silicon oxide was deposited over all the devices. Photo resist (PR) was evenly spun onto the wafer, developed to define the ridge waveguides, and then the developed PR was removed. The exposed silicon oxide was removed, leaving silicon oxide lines only where the ridge waveguides should be. PECVD of silicon nitride was then performed, to protect areas of the wafer from the following etch step. PR was again used to define the deep etch regions, and after the developed PR was removed, the areas which required a deep etch (including the metal covered etched facets and the pits) were etched to a depth of 1 μm by using an inductively coupled plasma (ICP) etcher. The silicon nitride was then removed, the ridge waveguide was defined and protected as in the previous steps, and a further 1.8 μm of material was etched. This process leaves the ridge waveguide's height at 1.8 μm, while leaving the areas of the pits and the metal covered etched facets a depth of 2.8 μm below the top of the ridge.

The fabrication process was then completed by depositing oxide over the whole device, leaving oxide openings only along the ridge, and evaporating a 400 nm thick mix of titanium and gold onto the devices for the electrical contact. The substrate was also thinned, and titanium and gold was also evaporated onto back of the thinned substrate for better contact. Scanning electron microscope (SEM) images of a pit can be seen in Fig. 5(a), and a side view of the two etch depths can be seen in Fig. 5(b). Further SEM images of the devices, including images of the metal covered etched facets, are included in the supplementary material.

The devices were tested by mounting each un-packaged chip on a temperature controlled brass chuck. Light from the un-coated cleaved facet of the devices was collected using a lensed fibre. A

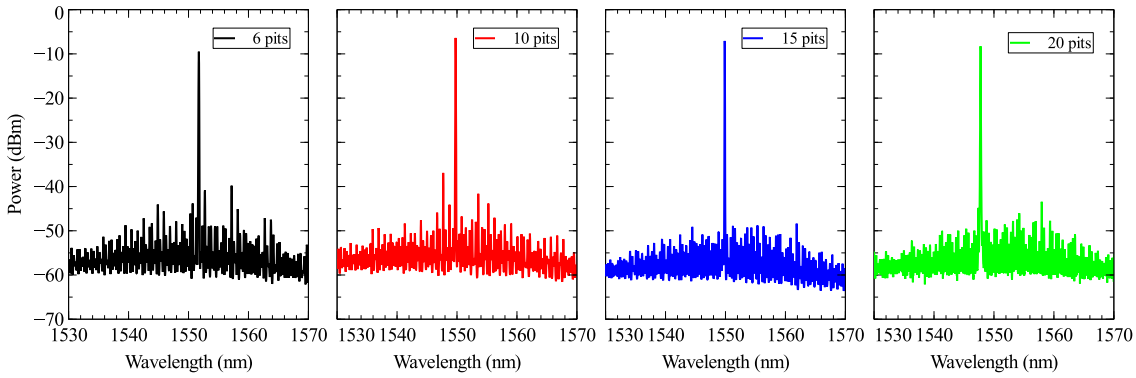

Fig. 7. Optical spectra from the fabricated devices, for the gratings shown in 3(b), at injected currents of 1.5 times threshold at 20 °C.

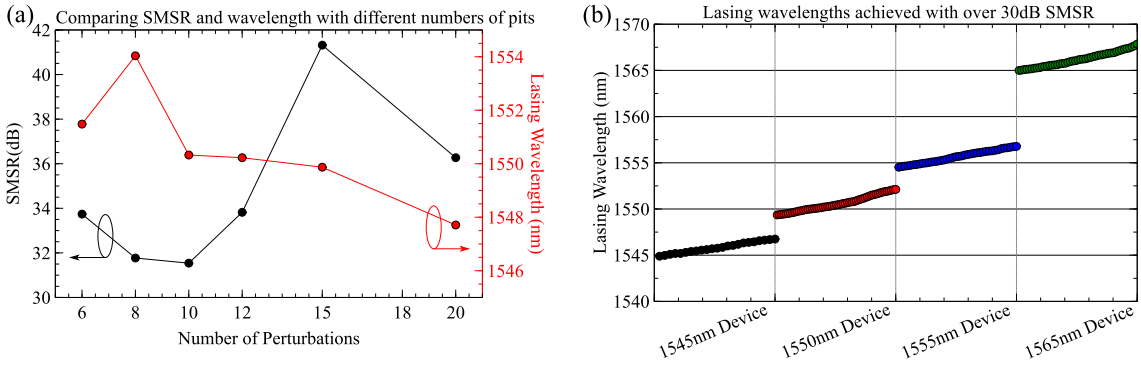

Fig. 8. (a) Comparison between the lasing SMSR and the lasing wavelength of devices as the number of pits was altered, at 20 °C. (b) Lasing wavelengths with over 30 dB SMSR from a set of devices designed to lase at 1545 nm, 1550 nm, 1555 nm, and 1565 nm.

comparison between the optical spectrum of a Fabry-Pérot laser and a device with 15 pits is shown in Fig. 6(a). The total length of both devices was 1 mm, and both were pumped with 140 mA.

The spectral effect of placing the pits as described by the inverse scattering method can be clearly seen, as strong single mode lasing is apparent upon the introduction of the pits.

To determine the optimal number of pits required for single mode lasing, the number of pits in a 1 mm cavity was varied. Figs. 6(b) and (c) show example IV and LI curves from devices with 6, 10, 15 and 20 pits. Each pit perturbations adds scattering losses to the laser cavity, and as a result the device thresholds increase from 37 mA at 6 pits to 53 mA at 20 pits. However, increasing the number of perturbations in the cavity also increases the wavelength selectivity and single mode behavior of the device.

The optical spectra from the same devices are shown in Fig. 7. All devices lased close to the target wavelength of 1550 nm, however the SMSR varies between devices. A summary of the SMSRs and the lasing wavelengths obtained as the number of pits was varied is plotted in Fig. 8(a). The lasing wavelength of the 6 and 8 pit devices aren't adequately close to the target wavelength, as neither had a sufficient number of perturbations to control the spectral characteristics of the device. However in the case of the 10, 12 and 15 pit devices, the lasing wavelengths of the devices at 20 °C were within 0.35 nm of the target wavelength. As the number of pits were increased further to 20, the wavelength accuracy of the design process was lost again. This can be explained as the increase in the number of pits can perturb the Fabry-Pérot modes of the 1 mm cavity away from their natural wavelengths, and the calculations assume that $N\Delta n/n \ll 1$. The model could be improved by taking into account the shift in the Fabry-Pérot mode positions, as well as taking into account second order perturbations [8].

Although the locations of the perturbations were fixed relative to the etched facet, the location of the cleaved facet on the uncoated hand side of the devices had a tolerance of approximately ± 10 μm. This error in the location of the cleaved facet affects more severely devices with fewer perturbations, as the threshold gain modulation isn't as strong in these cases.

Devices with 15 pits were fabricated to target wavelengths across the C band, to demonstrate the wavelength accuracy of the technique. Devices with target wavelengths of 1545 nm, 1550 nm, 1555 nm, and 1565 nm were designed and fabricated, and the lasing wavelengths achieved are shown in Fig. 8(b). The laser's wavelengths were tuned using both current (from 70 mA to 180 mA) and temperature (from 15 °C to 28 °C), and continuous tuning of 2 nm was achieved in all cases. These shifts observed in lasing wavelengths are due to the change in optical path lengths of the laser cavities, including the thermal expansion of the cavities and the slight variation in the refractive index of the material with temperature.

4. Conclusion

We have demonstrated regrowth-free monolithically integrable lasers, using deeply etched pits suitable for photonic integrated circuits. The pit perturbations used are etch depth independent, and have greater fabrication tolerances than the previous slotted devices reported. A preliminary study on how many perturbations are required to achieve high spectral efficiency was completed. It was found that SMSRs of greater than 40 dB can be achieved with as few as 15 pits, and the wavelength accuracy of the method was demonstrated across the gain bandwidth of the material used.

Acknowledgment

The authors would like to thank the anonymous reviewers for their valuable suggestions.

References

[1] D. Byrne *et al.*, "Discretely tunable semiconductor lasers suitable for photonic integration," *IEEE J. Sel. Topics Quantum Electron.*, vol. 15, no. 3, pp. 482–487, May/Jun. 2009. [Online]. Available: http://ieeexplore.ieee.org/document/4926148/

[2] B. Corbett and D. McDonald, "Single longitudinal mode ridge waveguide 1.3 μm Fabry-Perot laser by modal perturbation," *Electron. Lett.*, vol. 31, no. 25, pp. 2181–2182, Dec. 1995. [Online]. Available: http://digital-library.theiet.org/content/journals/10.1049/el_199514 87

[3] R. Phelan *et al.*, "A novel two-section tunable discrete mode Fabry-Perot laser exhibiting nanosecond wavelength switching," *IEEE J. Quantum Electron.*, vol. 44, no. 4, pp. 331–337, Apr. 2008. [Online]. Available: http://ieeexplore.ieee.org/document/4456801/

[4] Q. Y. Lu *et al.*, "Analysis of slot characteristics in slotted single-mode semiconductor lasers using the 2-D scattering matrix method," *IEEE Photon. Technol. Lett.*, vol. 18, no. 24, pp. 2605–2607, Dec. 2006. [Online]. Available: http://ieeexplore.ieee.org/document/4026621/

[5] M. Dernaika, N. Kelly, L. Caro, K. Shortiss, and F. Peters, "Regrowth-free single-mode semiconductor laser suitable for monolithic integration based on pits mirror," *Opt. Eng.*, vol. 56, no. 8, 2017, Art. no. 086107.

[6] J. J. Kelly and H. G. Philipsen, "Anisotropy in the wet-etching of semiconductors," *Current Opinion Solid State Mater. Sci.*, vol. 9, no. 1–2, pp. 84–90, Feb. 2005. [Online]. Available: https://www.sciencedirect.com/science/article/pii/S1359028606000283#fig2

[7] M. Dernaika *et al.*, "Deeply etched inner-cavity pit reflector," *IEEE Photon. J.*, vol. 9, no. 1, Feb. 2017, Art. no. 1500808.

[8] S. O'Brien, A. Amann, R. Fehse, S. Osborne, E. P. O'Reilly, and J. M. Rondinelli, "Spectral manipulation in Fabry-Perot lasers: Perturbative inverse scattering approach," *J. Opt. Soc. Amer. B*, vol. 23, no. 6, pp. 1046–1056, Jun. 2006. [Online]. Available: https://www.osapublishing.org/abstract.cfm?URI=josab-23-6-1046

[9] S. O'Brien *et al.*, "Design, characterization, and applications of index-patterned Fabry Pérot lasers," *IEEE J. Sel. Topics Quantum Electron.*, vol. 17, no. 6, pp. 1621–1631, Nov. 2011. [Online]. Available: http://ieeexplore.ieee.org/document/5755170/

[10] G. Adolfsson, J. Bengtsson, Å. Haglund, B. Nilsson, and A. Larsson, "Realization of spectrally engineered semiconductor Fabry-Perot lasers with narrow geometrical tolerances," *J. Appl. Phys.*, vol. 109, no. 9, May 2011, Art. no. 093112. [Online]. Available: http://aip.scitation.org/doi/10.1063/1.3587359

[11] S. O'Brien and E. P. O'Reilly, "Theory of improved spectral purity in index patterned Fabry-Pérot lasers," *Appl. Phys. Lett.*, vol. 86, no. 20, May 2005, Art. no. 201101. [Online]. Available: http://aip.scitation.org/doi/10.1063/1.1919389

[12] G. Adolfsson, J. Bengtsson, and A. Larsson, "Spectral engineering of semiconductor Fabry-Perot laser cavities in the weakly and strongly perturbed regimes," *J. Opt. Soc. Amer. B*, vol. 27, no. 1, pp. 118–127, Jan. 2010. [Online]. Available: https://www.osapublishing.org/abstract.cfm?URI=josab-27-1-118

[13] D. Bitauld, S. Osborne, and S. O'Brien, "Design of waveguide-integrated semiconductor laser sources for optical frequency comb generation," *Opt. Lett.*, vol. 36, no. 15, pp. 2985–2987, Aug. 2011. [Online]. Available: https://www.osapublishing.org/abstract.cfm?URI=ol-36-15-2985
[14] S. O'Brien, S. Osborne, D. Bitauld, and A. Amann, "Design and applications of discrete mode Fabry-Perot diode lasers," *Photon. Nanostructures— Fundamentals Appl.*, vol. 8, no. 4, pp. 218–227, Sep. 2010. [Online]. Available: https://www.sciencedirect.com/science/article/pii/S1569441010000490?via %3Dihub
[15] L. A. Coldren, S. W. Corzine, and M. Mashanovitch, *Diode Lasers and Photonic Integrated Circuits*. Hoboken, NJ, USA: Wiley, 2012.